Title

Shape-controlled synthesis and in situ characterisation of anisotropic Au nanomaterials using liquid cell transmission electron microscopy

Journal

Nanoscale, 11(36)

ISSN

2040-3364

Authors

Wang, Shih-Ting

Lin, Yiyang

Nielsen, Michael H

et al.

Publication Date

2019-09-19

DOI

10.1039/c9nr01474h

Peer reviewed

Shape-Controlled Synthesis and *In Situ* Characterisation of Anisotropic Au Nanomaterials using Liquid Cell Transmission Electron Microscopy

Shih-Ting Wang[†‡∥], Yiyang Lin[†‡§], Michael H. Nielsen[⊥], Cheng Yu Song[∥], Michael R. Thomas[†‡§], Christopher D. Spicer[†‡§], Roland Kröger[▽], Peter Ercius[∥], Shaul Aloni[∥], and Molly M. Stevens[*†‡§]

[†]Department of Materials, Imperial College London, Exhibition Road, London, SW7 2AZ, United Kingdom

[‡]Department of Bioengineering, Imperial College London, London, SW7 2AZ, United Kingdom

[§]Institute of Biomedical Engineering, Imperial College London, London, SW7 2AZ, United Kingdom

[⊥]Physical & Life Sciences Directorate, Lawrence Livermore National Laboratory, 7000 East Avenue, Livermore, California, 94550, United States

[∥]Molecular Foundry, Lawrence Berkeley National Laboratory, 1 Cyclotron Road, Berkeley, California, 94720, United States

[▽]Department of Physics, University of York, Heslington, YO5 10DD, United Kingdom

ABSTRACT

Understanding the mechanisms behind crystal nucleation and growth is a fundamental requirement for the design and production of bespoke nanomaterials with controlled sizes and morphologies. Herein, we select gold (Au) nanoparticles as the model system for our study due to their representative applications in biology, electronics and optoelectronics. We investigate the radiation-induced *in situ* growth of gold (Au) particles using liquid cell transmission electron microscopy (LCTEM) and study the growth kinetics of non-spherical Au structures. Under controlled electron fluence, liquid flow rate and Au^{3+} ion supply, we show the favoured diffusion-limited growth of highly-twinned nascent Au seed particles into branched structures when using thin liquid cells (100 nm and 250 nm) in LCTEM, whereas faceted structures (*e.g.*, spheres, rods, and prisms) formed when using a 1 µm thick liquid cell. We propose that the diffusion-controlled branched Au particle growth in the thin liquid cells results from the lower number and twinning of nascent seed particles. In addition, we observed

that anisotropic Au growth could be modulated by Au-binding amyloid fibrils, which we ascribe to their capability of regulating Au^{3+} ion diffusion and mass transfer in solution. We anticipate that this study will provide new perspectives on the shape-controlled synthesis of anisotropic metallic nanomaterials using LCTEM.

KEYWORDS: Liquid cell TEM, *in situ* growth, diffusion-limited growth, branched structures, amyloid fibrils.

INTRODUCTION

Controlling the morphological features of metal nanocrystals is crucial to provide the flexibility required to engineer their catalytic, electronic and optical properties. Advancements in colloidal synthesis have led to the production of a variety of metal nanocrystals with different shapes and sizes (*e.g.* spheres, rods, cubes, plates, prisms and stars) as building blocks, which can be assembled into complex nanoscale devices and applications.[1-4] Among these structures, branched particles are of great interest as they combine polarisation-dependent light scattering and strong dielectric sensitivity into a single structure.[5] In addition, branched metal particles can be developed into nanoantennas, where plasmonic properties can be tailored by controlling the number and angle of the prongs, promoting the reception/transmission of light at the nanoscale.[1, 5-7] However, controlled growth of such anisotropic crystal structures is typically difficult to achieve without the use of capping reagents to direct growth, due to the similar surface free energies of major crystal facets.[2, 8-11] It is therefore crucial to understand the role of shape-controlling factors for branched particles and unveil the fundamental growth mechanisms in dynamically changing solution environments.[12] For example, microfluidic devices have been developed as new tools to synthesise monodispersed anisotropic nanocrystals by controlling the mixing, reaction times and flow rates of different reagents.[13-15] A major challenge in this research field arises from the lack of characterisation tools for direct visualisation of the chemical and physical events occurring in liquid environments during crystal growth.

The recent development of *in situ* liquid cell transmission electron microscopy (LCTEM) provides an opportunity to explore new frontiers in electrochemistry, catalysis, nanocrystal growth, fluid physics, radiation physics and complex soft materials in aqueous environments.[16-23] In particular, this technique can complement

spectroscopy and X-ray based methods to track nanoparticle (NP) growth trajectories through direct visualisation of crystal formation in liquid environments, with a unique combination of temporal and spatial resolutions.[6, 16, 18, 20, 22, 24-33] On the other hand, the irradiating electrons can change the solution chemistry in the submicron layer of liquid encapsulated between two electron transparent membranes (*e.g.*, silicon nitride or graphene), by creating transient radical products, including e_h^- (hydrated electrons), $H^\bullet$, $OH^\bullet$, H_2O_2 and H_3O^+.[20, 34-36] Among these reactive species, e_h^- are known to reduce metal ions and initiate crystal growth in solution or on the silicon nitride (Si_xN_y) membranes of the liquid cell.[35-37] Recent studies have shown that through control of electron fluence and solution composition, mechanistic information on crystal growth can be extracted, with results that resemble those from bench-top chemical syntheses.[38, 39] For example, graphene liquid cells have been used to study platinum nanocrystal growth by electron beam irradiation, in which critical steps in some crystal growth pathways, including orientated attachment and cluster coalescence were visualised at the atomic scale.[12, 38] In addition, results obtained from LCTEM suggest that nanocrystal shape evolutions and their final morphologies strongly depend on the nascent cluster structures, growth rate of different crystallographic facets, and mobility and concentrations of surface ligands.[40, 41] However, NP growth in LCTEM, particularly in open-flow systems still requires further exploration due to the multivariate nature of the experiments, where factors such as electron fluence,[32, 42] flow dynamics,[43-46] solution chemistry,[25, 32] liquid cell designs,[47, 48] radiolysis/thermal effects can,[20, 49, 50] to differing extents, influence imaging resolution, NP growth kinetics and final NP morphologies.

Here, we present LCTEM experiments exploring the development of a range of Au particle morphologies formed by electron beam irradiation-induced reduction of Au ions (Au^{3+}) into colloidal Au (Au^0) in aqueous solution. The implementation of a continuous flow within an *in situ* liquid stage allowed us to image during stepwise injection of the aqueous components, and to maintain a constant external flow rate and supply of the gold chloride ($HAuCl_4$) precursor solution.[51, 52] By analysing particle growth rates, *in situ* shape transformations and crystallographic structures of the electron beam-induced seeds and the resulting Au particles, we demonstrate that liquid layer thickness is an important factor linked to the resulting Au morphology. A hypothesis was made to illustrate the role of liquid layer thickness in affecting Au^{3+}

mass transfer/diffusion and diffusion-limited growth into branched Au structures. We further investigated the anisotropic Au growth by introducing Au-binding amyloid fibrils from islet amyloid polypeptide (IAPP), for which we proposed that the strong peptide-Au affinity mediates Au^{3+} diffusion and influences the Au growth kinetics. Combined with the results of our amyloid-free, controlled environment *in situ* LCTEM studies, we discuss the power of physical and chemical conditions in determining anisotropic metal nanocrystal growth and shape evolution, which we believe will find applications in the fields of biotechnology, biomineralisation and crystal growth.

RESULTS AND DISCUSSION

We performed crystal growth experiments in a single inlet and single outlet liquid cell stage (Hummingbird Scientific), inserted into a field-emission JEOL 2100F TEM and operated at an acceleration voltage of 200 keV (see Methods).[53] Imaging was conducted in TEM mode with a 5 μm diameter beam irradiating a cylinder of liquid solution containing Au(III) chloride ($HAuCl_4$), and recorded at one frame per second at a low magnification (5000x). Au^{3+} reduction by electron beam irradiation was performed at a dose rate of ~1.78 $e^-/Å^2 \cdot s$ to control the reduction process and prevent bubble formation in the liquid chamber (**Figure S1**). This undesired phenomenon is known to arise from localised heating or radiolysis during the electron-liquid interactions.[25, 50] In addition, imaging of particle growth in the liquid-filled cells was primarily performed at or near the edge of the Si_xN_y windows to minimise significant elastic deformation at the centre of the windows, which originates from the pressure differences between the liquid-filled cell and the high vacuum of the microscope column.[52, 54]

During electron beam irradiation in the LCTEM using a spacer thickness of 250 nm, we observed immediately the formation of Au particles with diameters of 5–10 nm on the Si_xN_y windows, and branched particles (0.5−1 μm) were visualised after irradiating for 15 sec (**Figure 1a and Movie S1**). The growth rate of branched Au particles can be evaluated by plotting the 2D-projected area of the particles as a function of time (**Figure S2**), and the particle growth curve fits well (R^2 = 0.98) with an exponential function, suggesting fast growth kinetics (**Figure 1b**). According to the Lifshitz-Slyozov-Wagner (LSW) power model, particle growth kinetics can be presented as $r \propto t^n$ (or $A \propto t^\beta$, where $\beta = 2n$), where r is the radii, A is the 2D-projected area of the particles and t is the experimental time frame. In **Figure S3**, the growth

kinetics exhibited a $\beta = 0.634$ dependence and therefore $n \sim 0.32$, which approximates to a diffusion-limited growth.[55] Note that in **Figure S3**, the growth curve fitted well within the accelerated growth regime (180 sec), while deviation from the growth trajectory was observed afterward. We propose that this is due to the confined growth in the *z*-direction and continuous Au^{3+}supply in the open flow system. The electron dose rate is an important factor that influences nanoparticle growth in liquid-cell TEM. According to Zhang *et al.*,[32] a higher electron dose rate (> 0.5 $e^-/Å^2 \cdot s$) favours the formation of dendritic Au nanostructures *via* diffusion-limited growth when using 1 mM of $HAuCl_4$. In this work, we obtained anisotropic Au nanostructures from diffusion-limited growth using an electron dose rate of 1.78 $e^-/Å^2 \cdot s$ and 1 mM of $HAuCl_4$, which agrees with the findings reported by Zhang and colleagues.[32]

In **Figure 1c, d**, a branched Au particle with three facets, {200}, $\{1\bar{1}1\}$, and $\{\bar{1}\bar{1}1\}$, with a defined twin boundary at Au{111} at the tip of the branch can be observed. Selected area electron diffraction (SAED) confirmed the twinned structure in a single Au particle (**Figure S4**). We also observed a penta-twinned structure on a branched Au particle by scanning transmission electron microscopy (STEM) imaging (**Figure 1e**). Previous findings have shown that twinning causes an increased strain in the lattice and provides the necessary symmetry breaking, which results in subsequent elongation toward unstrained directions.[56-59] We therefore propose that twin boundaries formed during particle growth at the early stage (*i.e.*, nascent seed particles, **Figure S5**) play a crucial role in determining the development into anisotropic structures.

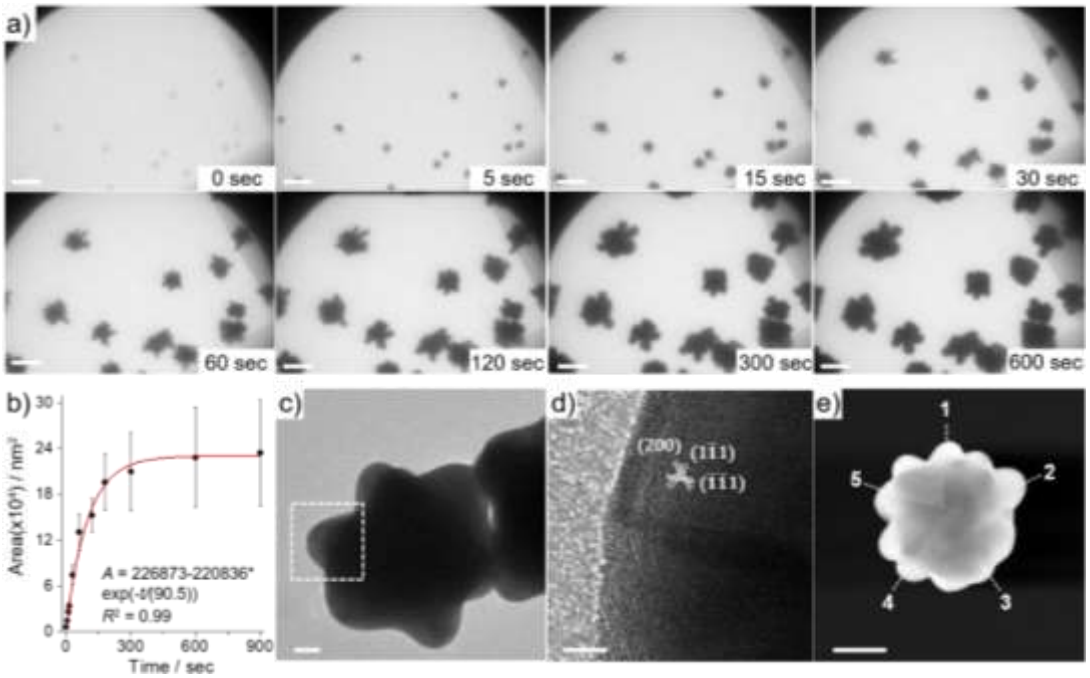

Figure 1 (a) Snapshots of an *in situ* LCTEM experiment show the formation of branched Au particles within 600 sec in a 250 nm liquid cell (scale bars: 500 nm). (b) 2D-projected areas of the Au particles plotted against time show the growth kinetics of the branched structures. The error bars represent standard deviation (n = 5). Post-mortem (c) TEM, (d) high resolution TEM (HRTEM) and (e) STEM images of the branched Au particles show the multi-twinned structure and the twin boundary at Au{111} at the tip of the branch. Scale bars: (c) 50 nm, (d) 2 nm, (e) 100 nm.

We also observed the formation of branched particles 1−2 µm away from the electron beam irradiation area (**Figure S6**). TEM images were taken at regions perpendicular to the beam path and along the direction of the liquid flow after 15 min of electron beam irradiation at the window corner. We propose that this is likely due to the migration of scattered electrons along the Si_xN_y windows and in liquid, along with the rapid diffusion of e_h^- (diffusion coefficient: ~5 x 10^{-5} cm^2/s)[60, 61] under thermodynamic equilibrium,[50, 51, 62, 63] which triggered growth of branched Au particles close to the irradiated area. In addition, the liquid flow could remove e_h^- and radiation-induced Au(0) outside the irradiation areas, causing the formation of Au particles.[32] Beyond 2 µm away (up to ~8 µm) from the irradiation area, Au prisms, rods, and spheres were formed while no branched Au particles were observed (**Figure S6**). We propose that formation of varied Au morphologies at different positions (**Figure S6**) are likely due to the variation of liquid layer thicknesses and thereby liquid flow patterns, which affect the Au growth kinetics.[44, 45, 48] This phenomenon is similar to the finding in microfluidic devices, where NP synthesis can be affected by changing the flow parameters.[13-15, 64] However, the mechanism behind it is difficult to explore under *in-situ* LCTEM. This requires further studies on the axial dispersion in a single-phase flow across the liquid cell and controlled NP growth under varied flow rates.

Formation of Au prisms and rods could be found to grow from different shapes of the early formed seed particles in the 250 nm cell. Note that the seed particles were pre-formed in areas without direct electron beam irradiation and were likely to be radiation-induced Au(0) removed from the irradiation area by the liquid flow.[32] **Figure 2** shows the morphological transitions from triangular to a truncated hexagonal shape and from rectangular to a rod-like Au structure in LCTEM. TEM and SAED analyses suggested that the non-branched Au rods grew in the <110> directions, when observed

from the [$1\bar{1}2$] direction (**Figure 2b, c**). Similarly, 2D triangular and hexagonal structures displayed growth in the <110> directions (**Figure 2d−g**), suggesting that hexagonal-shaped Au prisms were likely evolved from triangular or truncated hexagonal Au prisms. This also supports that the final Au particle morphologies are determined by the nascent seed particles.[9]

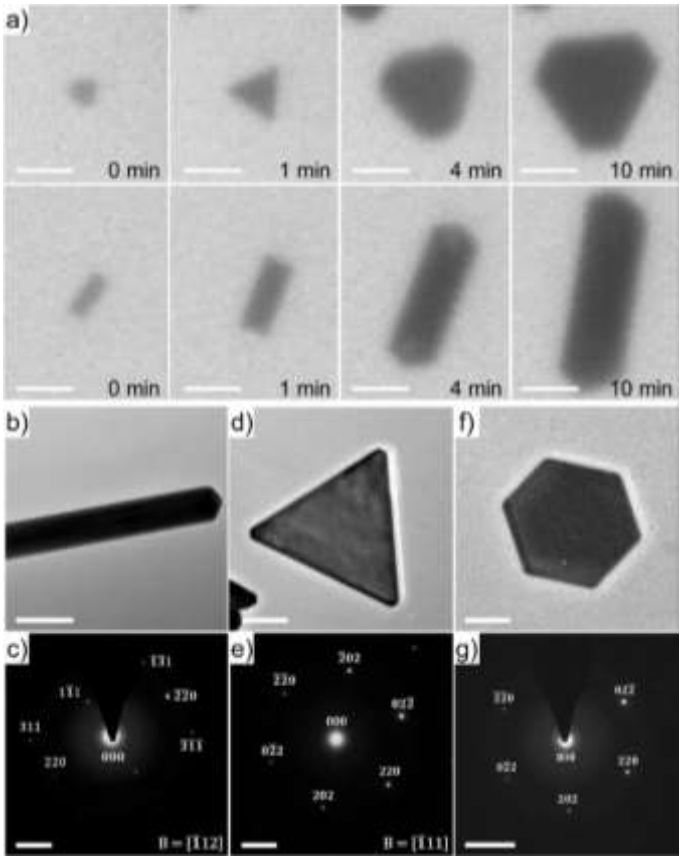

Figure 2 (a) LCTEM image sequences show shape transformations from triangular into truncated hexagonal Au prisms and rectangular into Au rods in a 250 nm liquid cell (scale bars: 500 nm). (b, d, f) *Post-mortem* TEM analyses and (c, e, g) SAED patterns of Au rods (b, c) and 2D Au prisms (d-g) formed by the *in situ* LCTEM experiments in a 250 nm liquid cell. The SAED patterns show growth in the <110> directions. Scale bars: (b) 100 nm, (d, f) 200 nm, (c, e, g) 5 1/nm.

We further found that Au growth was affected by changing the spacer thicknesses (100 nm, 250 nm, and 1 μm) of the liquid cells, while maintaining external parameters including the electron fluence, external liquid flow rate and supply of the $HAuCl_4$ precursor solution. **Figure 3a** shows *in situ* growth in a 1 μm liquid cell, where the experimental parameters and J_c of the electron beam were kept consistent with the experiments presented in **Figure 1** using a 250 nm liquid cell. Immediately upon

electron beam irradiation, we observed small Au particles (~5 nm) in solution (**Figure 3a and Movie S2**). After ~120 sec, Au spheres (≤ 0.2 μm) as well as Au rods and 2D prisms began to form while branched Au particles were not observed. The growth kinetics of Au rods (**Figure S7**) determined by plotting 2D-projected area as a function of time (**Figure 3b**) showed the gradual growth over time.

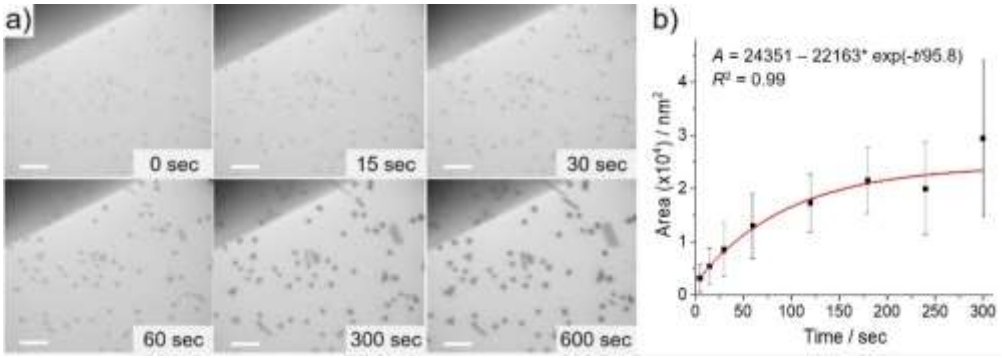

Figure 3 (a) Snapshots of *in situ* LCTEM experiment show the formation of spherical and faceted Au particles (*i.e.*, prisms and rods) in a 1 μm liquid cell (scale bars: 500 nm). Shape transformations of Au prisms (*e.g.*, triangle to hexagons) and elongation of Au rods were observed in 600 sec. (b) 2D-projected areas of the Au rods plotted against time across the *in situ* experiment in **Figure S6**. The error bars represent standard deviation (n = 6).

When using a smaller spacer (100 nm), anisotropic growth of the Au seed particles into branched structures was observed. These branched Au particles (>4 particles) displayed sharper tips and larger particle sizes (0.5−2 μm) (**Figure 4, S8 and Movie S3**), compared to those seen in the 250 nm liquid cell (**Figure 1**). In addition, multiple twin boundaries, including penta-, hexa- or higher-order twinned structures can be seen in the electron beam-induced Au seed particles, which agrees with the finding that the presence of twinned facets favoured branched Au structures (**Figure S9**).[58] In particular, rapid growth of the branches in the 100 nm liquid cell resulted in a polycrystalline structure (**Figure S10**) and led to tip splitting and development of new branches (**Figure 4**), which was not observed in the branched particles formed in the 250 nm liquid cell (**Figure 1**). We note that electron-liquid interactions can cause complex fluid behaviours in the 100 nm cell and result in non-thermodynamic conditions and kinetic growth of the Au particles.[25] The liquid flow may also assist Au nucleation and growth outside the irradiation area.[32] For example, we observed occurrence of electron beam-induced ion diffusion under LCTEM, which produced Au

seed particles at the periphery of the electron beam irradiation area (**Figure S11**). This phenomenon has been reported to trigger nucleation and growth of lead sulphide NPs in a region surrounding the initial electron beam irradiation.[25]

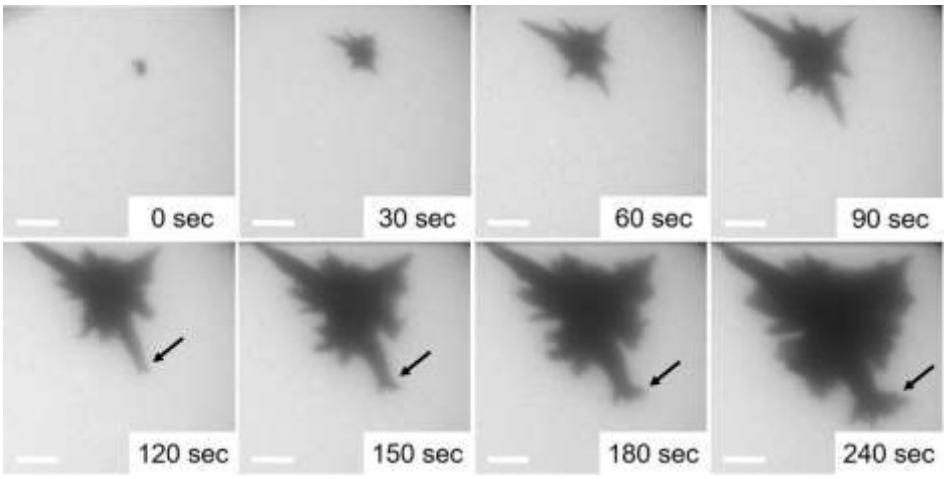

Figure 4 Snapshots of *in situ* LCTEM show the formation of branched Au particles in the 100 nm liquid cell, where fast growth at the Au branches was observed and followed by splitting of the Au branches. Note that the Au seed particle at 0 sec was pre-formed on the liquid cell window. The splitting of the Au branches from 120 sec was indicated by arrows (scale bars: 500 nm).

As shown above, the striking differences in electron beam irradiation-induced Au growth was primarily caused by changing the thickness (100 nm, 250 nm and 1 μm) of liquid cells (**Figure 5**). All the LCTEM experiments were conducted under a constant flow (5 μL/min) of fresh $HAuCl_4$ precursor solution under the same concentration. By foregoing the use of templating surfactant molecules, we sacrifice a degree of control over size and shape distribution of nanocrystals. However, with our simplified approach, we can propose three factors that may contribute to the formation of large branched Au particles in the 100 nm and 250 nm liquid cells. First, the twinning of nascent seed particles formed in LCTEM (**Figure S4, S5 and S9**) increases lattice strain and provides symmetry breaking to induce anisotropic growth of branched Au particles.[56-58] Second, the fast diffusion-limited growth of Au particles in thin liquid cells tends to induce anisotropic overgrowth, since the atomic addition is faster than diffusion along the low-energy facets (*e.g.*, {111}). Oppositely, at lower growth rates, crystals may undergo relaxation during the growth process to minimise the total surface energy,[34] and likely form polyhedral structures with high-energy facets such as the {100} and {110} planes.[5, 65, 66] Third, the lower number of Au seed particles in the 100 nm cell is

another factor leading to anisotropic Au growth and the formation of larger particles (**Figures 1, 3 and 4**). According to the literature,[2, 67-69] reducing the number of seed particles promotes anisotropy of gold nanorods and nanostars and increases the sizes of the branched Au structures. It is therefore reasonable that large branched Au structures were the energetically favoured products from diffusion-limited growth when using thin liquid cells.

In particular, under externally-controlled liquid injection, the liquid flow rate in a thin cell is supposed to be higher than that in a thick cell, which subsequently removed the radiation-induced Au(0) by the liquid flow.[32] This will reduce the probability of Au seed formation in thin cells and thereby lower the seed numbers in solution as shown in **Figure 1a and 3a**. In addition, the internal liquid flow rates may influence the reaction rates between Au^{3+} precursor and the reducing e_h^-, residence time, as well as interactions between Au nuclei. Moreover, to reach the critical nucleus size to continue growth under such condition, the Au seed particles were more likely to form through a rapid reaction which favoured the formation of fivefold or higher-fold twinning of the seed particles (**Figure 1e, S4, S5 and S9**).[70, 71] However, further studies are required to reveal the effect of internal and external flow rates of the open flow system toward NP nucleation and growth kinetics.

One may also argue that the concentration of the main reducing species, e_h^- could vary when changing the size of the liquid cells. This possibility could be excluded since e_h^- were majorly generated at a distance of approximately 10 nm or less at the Si_xN_y window/liquid interface, and therefore independent of the thicknesses of the liquid cells that were much larger than the size.[72, 73]

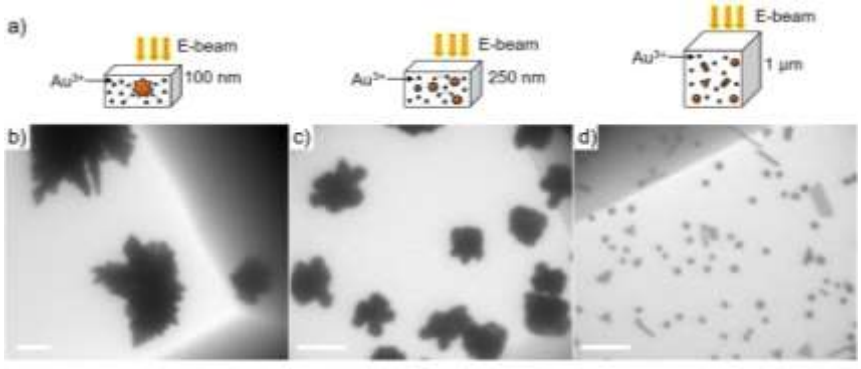

e) Spacer	Growth rate	Morphology	Structure
100 nm	Fast	Sharply branched/dendritic	Polycrystalline
250 nm	Medium	Branched	Twinned
1 µm	Slow	Prisms and rods	Faceted/twinned (rods)

Figure 5 (a) Schematic view shows the proposed relationship between liquid thickness and Au growth rate as well as the final particle morphology. Diffusion-limited growth into branched Au particles in thin liquid cells is proposed to be due to the lower number of Au seed particles and enhanced ion diffusion. (b–d) LCTEM images of different Au morphologies formed during the *in situ* experiment using varied thicknesses of the liquid cell spacers: (b) 100 nm (scale bar: 1 μm), (c) 250 nm (scale bar: 500 nm) and (d) 1 μm (scale bar: 500 nm). (e) Summary of the Au growth rate, morphologies and structures observed for different liquid thicknesses.

Finally, we investigated the role of Au^{3+} mass transfer in the growth and reshaping of Au particles. This was studied by employing an Au-binding biological template. Previously, nucleation and growth of calcium carbonate crystals immobilised in a biomimetic polystyrene sulphonate (PSS) matrix was reported to be restricted by the Ca^{2+}–PSS binding.[74] Here, an Au-binding islet amyloid polypeptide (IAPP), a type II diabetes related amyloid peptide was selected, where we have previously observed that the synergistic effect of electrostatic forces, multivalent Au-amine coordination, and Au–thiol bonding drive IAPP–Au interactions preferentially on the {111} surfaces and accelerates peptide self-assembly into fibrils.[11]

Initially, mature IAPP fibrils capable of binding Au NPs were produced (**Figure S12**) and their adhesion to Si_xN_y surfaces were established *ex situ* (**Figure S13**). To study the effect of Au-binding IAPP on the formation of branched Au structures *in situ*, we deposited IAPP fibrils on the 250 nm spacer window, assembled the cell and were able to confirm their adhesion by LCTEM imaging of the negatively stained fibrils (**Figure S14a**), and those stained by premixing the fibrils with 5 nm Au NPs (**Figure S14b**). Larger fibril aggregates were, however, visible in the LCTEM without staining even in the presence of strong electron scattering from the liquid layer and a low contrast of individual fibrils (**Figure S14c**). Immediately after electron beam irradiation, a large number of Au seeds were resolvable, which underwent growth into particles of diameters up to 0.2 μm after electron beam irradiation for 5 min (**Figures 6a**, **6c**, **S15 and Movie S4**). It is worth noting that the existence of IAPP fibrils could also be observed in the movement of the Au-"stained" fibrils in liquid. As expected, we observed aggregation of IAPP fibrils under the cumulative electron flux (**Figure S15**), possibly due to the denaturing effects of the electron beam on biomolecule structures.[75]

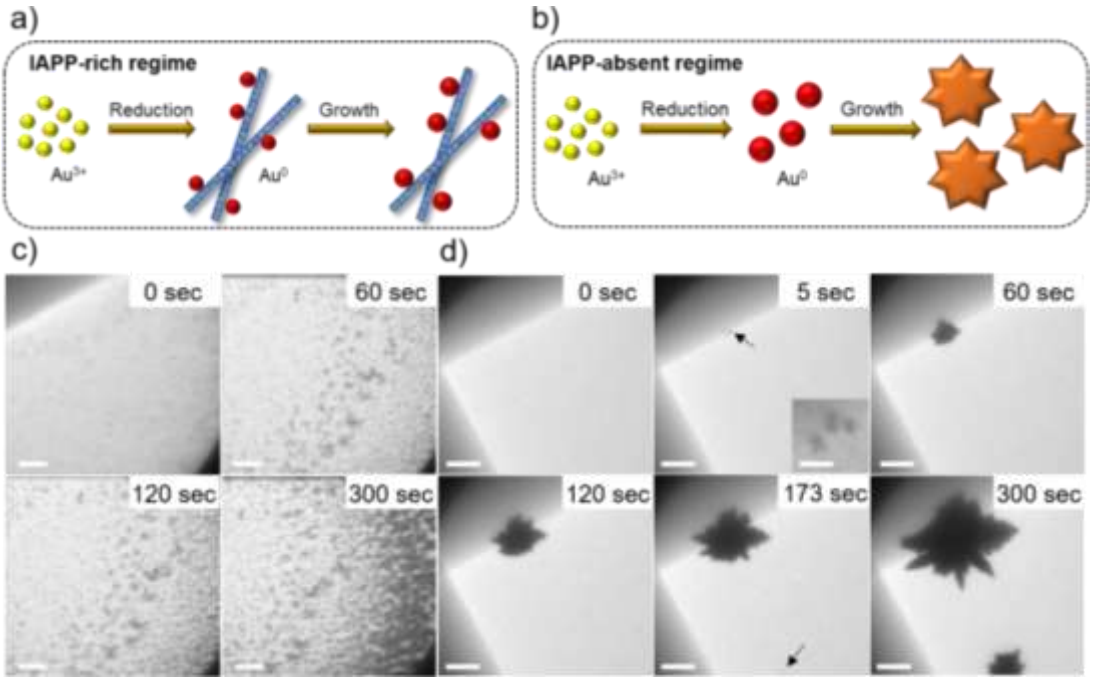

Figure 6 (a, b) Schematic view of the proposed mechanism of Au growth and final morphology in the presence and absence of IAPP fibrils. The surface of Au-binding amyloid fibrils provides multiple nucleation sites which reduce the local Au^{3+} concentration and prevents the formation of branched Au particles. (c, d) Snapshots of the *in situ* LCTEM experiment (250 nm liquid cell) show the formation of (d) particles ($\leq$ 0.2 μm) in the presence of IAPP fibrils and (d) branched Au particles (~2 μm) in the absence of fibrils. In (c), the nucleation-growth process begins immediately upon electron beam irradiation, whereas in (d), the first crystal was observed after a few seconds of irradiation and the second crystal was observed at 173 sec (arrow). Scale bars: 500 nm. The magnified inset image and arrow at 5 sec in (d) show coalescence of three Au particles that further grow into a large branched particle (scale bar: 100 nm).

Interestingly, we observed growth of large branched Au particles (~2 μm) in the same experimental time (300 sec) rather than small aggregated particles in the region where IAPP fibrils were not present (**Figures 6b, 6d, S16, S17 and Movie S5**). As shown in **Figure 6d**, the first branched Au particle formed by coalescence of three individual particles within 30 sec. The dendritic morphology is likely due to the surface reconstruction of multiple crystal domains, followed by diffusion-limited growth. We visualised subsequent branched particle formation after electron beam irradiation for ~170 sec (**Figure 6d**). The short delay for growth of the second particle may be due to rapid Au^{3+} localisation at the surface of the first particle. In repeat experiments and

imaging at different areas in a liquid cell (**Figures S16 and S17**), we found that small particles (0.02−0.2 μm) formed in the presence of IAPP fibrils, while the formation of branched Au particles (0.5−2 μm) occurred in the absence of fibrils. Therefore, we propose that the strong IAPP-Au affinity reduced local Au^{3+} diffusion and mass transfer to higher energy facets, inhibiting subsequent growth into branched Au structures. In addition, since the fibrils heterogeneously aggregate on the window surface, the highly localised concentration of peptide absorbs Au nuclei indiscriminately despite the preferential binding toward the Au{111}facets, preventing Au growth anisotropy. Such effects of peptide concentration on the size and morphologies of Au structures have also been reported in *ex-situ* Au growth by chemical reduction.[76]

CONCLUSIONS

In conclusion, we investigated the kinetics of electron beam-induced Au growth in aqueous solution using *in situ* LCTEM and demonstrated the important role of liquid cell thickness in directing the shape evolution of Au structures. Controlled growth of branched Au structures was achieved using a minimum liquid layer thickness of 100 nm and 250 nm, while Au spheres, rods or prisms were formed in a minimum layer thickness of 1 μm. We propose that the multi-twinned structures of Au seed particles and the favoured diffusion-limited growth are the main factors directing growth of branched Au particles, and that this phenomenon may be related to varied internal flow rates when using different sizes of the liquid cells. Real-time shape evolutions of the Au prisms and rods recorded by LCTEM showed growth in the <110> directions. Finally, by introducing Au-binding amyloid fibrils, the anisotropic Au growth and the resulting morphology could be manipulated, where we propose that the multiple Au-binding sites on the fibril surface reduce local Au^{3+} diffusion and growth anisotropy, inducing the formation of small Au particles (≤ 0.2 μm). This work reports the direct *in situ* LCTEM observation of electron beam-induced Au particle anisotropy, and the ability of Au-binding amyloid fibrils to restrict this anisotropic growth. Recently, Zhang and Erni showed that the growth mechanism and ultimate morphology of Au NPs could be tailored by tuning the electron dose rate, solute concentration, imaging mode, and liquid cell setup (static *vs* flow mode) using *in situ* LCTEM.[32] We highlight the important role of LCTEM experimental design, and the role of a macromolecule template directing *in situ* nanomaterial nucleation/growth. We anticipate that this

approach will expand the applicability of LCTEM to study dynamic processes in nanotechnology and biology at the single particle level.

AUTHOR INFORMATION

Corresponding Author

*E-mail: m.stevens@imperial.ac.uk

NOTES

The authors declare no competing financial interest.

ACKNOWLEDGEMENT

S.-T.W. thanks the financial support by Taiwan Strategic Alliance scholarship (UK-ICL-102-S03) and the Mobility Research Fellowship from the Engineering and Physical Sciences Research Council (EPSRC) Interdisciplinary Research Centre (IRC) "Early-Warning Sensing Systems for Infectious Diseases" (EP/K031953/1). M.M.S. and M.R.T. acknowledge support from the i-sense EPSRC IRC in Early Warning Sensing Systems for Infectious Diseases (EP/K031953/1; www.i-sense.org.uk). M.M.S. and Y.L. acknowledge support from the ERC Seventh Framework Programme Consolidator grant "Naturale CG" (616417). M.H.N. acknowledges support from the Lawrence Fellowship. M.M.S. acknowledges support from the EPSRC grant "Bio-functionalised nanomaterials for ultrasensitive biosensing" (EP/K020641/1). P.E. thanks the support from Office of Science, Office of Basic Energy Sciences, Materials Sciences and Engineering Division of the U.S. Department of Energy under Contract No. DE-AC02-05CH11231 within the KC22ZH program. LCTEM and conventional TEM imaging performed at the Molecular Foundry, Lawrence Berkeley National Laboratory were supported by the Office of Science, Office of Basic Energy Sciences, of the U.S. Department of Energy under Contract No. DE-AC02-05CH11231. Aspects of this work were performed under the auspices of the U.S. Department of Energy by Lawrence Livermore National Laboratory under Contract No. DE-AC52-07NA27344. We are grateful to Dr. Laura Rodriguez-Lorenzo and Dr. Qu Chen for critical reading of the manuscript and useful advice.

Supporting Information Available: Materials and experimental methods; LCTEM movies; TEM/LCTEM images and diffraction patterns of the Au particles from *in situ* and *ex situ* experiments; Thioflavin T fluorescence assay and circular dichroism analyses of the IAPP fibrils. All the supplementary movies were accelerated 10.05 times using AVS Video Editor.

REFERENCES

1. C. J. Murphy, T. K. Sau, A. M. Gole, C. J. Orendorff, J. Gao, L. Gou, S. E. Hunyadi and T. Li, *J. Phys. Chem. B*, 2005, **109**, 13857-13870.
2. M. Grzelczak, J. Perez-Juste, P. Mulvaney and L. M. Liz-Marzan, *Chem. Soc. Rev.*, 2008, **37**, 1783-1791.
3. B. Lim and Y. Xia, *Angew. Chem. Int. Ed.*, 2011, **50**, 76-85.
4. M. R. Jones, K. D. Osberg, R. J. Macfarlane, M. R. Langille and C. A. Mirkin, *Chem. Rev.*, 2011, **111**, 3736-3827.
5. C. L. Nehl, H. Liao and J. H. Hafner, *Nano Lett.*, 2006, **6**, 683-688.
6. J. Hun Park, M. C. Reuter, S. Kodambaka and F. M. Ross, *Microsc. Microanal.*, 2014, **20**, 1598-1599.
7. E. Hao, R. C. Bailey, G. C. Schatz, J. T. Hupp and S. Li, *Nano Lett.*, 2004, **4**, 327-330.
8. Y. Sun and Y. Xia, *Science*, 2002, **298**, 2176-2179.
9. Y. Xia, Y. Xiong, B. Lim and S. E. Skrabalak, *Angew. Chem. Int. Ed.*, 2009, **48**, 60-103.
10. N. T. K. Thanh, N. Maclean and S. Mahiddine, *Chem. Rev.*, 2014, **114**, 7610-7630.
11. S.-T. Wang, Y. Lin, N. Todorova, Y. Xu, M. Mazo, S. Rana, V. Leonardo, N. Amdursky, C. D. Spicer, B. D. Alexander, A. A. Edwards, S. J. Matthews, I. Yarovsky and M. M. Stevens, *Chem. Mater.*, 2017, **29**, 1550-1560.
12. J. J. De Yoreo, P. U. P. A. Gilbert, N. A. J. M. Sommerdijk, R. L. Penn, S. Whitelam, D. Joester, H. Zhang, J. D. Rimer, A. Navrotsky, J. F. Banfield, A. F. Wallace, F. M. Michel, F. C. Meldrum, H. Cölfen and P. M. Dove, *Science*, 2015, **349**, aaa6760.
13. S. Duraiswamy and S. A. Khan, *Small*, 2009, **5**, 2828-2834.
14. Y. Song, J. Hormes and C. S. S. R. Kumar, *Small*, 2008, **4**, 698-711.
15. V. Sebastian Cabeza, S. Kuhn, A. A. Kulkarni and K. F. Jensen, *Langmuir*, 2012, **28**, 7007-7013.
16. N. de Jonge and F. M. Ross, *Nat. Nanotechol.*, 2011, **6**, 695-704.
17. F. M. Ross, *Science*, 2015, **350**, aaa9886.
18. H.-G. Liao and H. Zheng, *Annu. Rev. Phys. Chem.*, 2016, **67**, 719-747.
19. J. H. Park, D. A. Steingart, S. Kodambaka and F. M. Ross, *Sci. Adv.*, 2017, **3**, e1700234.
20. T. J. Woehl and P. Abellan, *J. Microsc.*, 2017, **265**, 135-147.
21. S. F. Tan, S. W. Chee, G. Lin and U. Mirsaidov, *Acc. Chem. Res.*, 2017, **50**, 1303-1312.
22. R. Ramachandramoorthy, R. Bernal and H. D. Espinosa, *ACS Nano*, 2015, **9**, 4675-4685.
23. N. d. Jonge, D. B. Peckys, G. J. Kremers and D. W. Piston, *Proc. Natl. Acad. Sci.*, 2009, **106**, 2159-2164.

24. M. J. Williamson, R. M. Tromp, P. M. Vereecken, R. Hull and F. M. Ross, *Nat. Mat.*, 2003, **2**, 532-536.
25. J. E. Evans, K. L. Jungjohann, N. D. Browning and I. Arslan, *Nano Lett.*, 2011, **11**, 2809-2813.
26. T. Kraus and N. de Jonge, *Langmuir*, 2013, **29**, 8427-8432.
27. J. H. Park, N. M. Schneider, J. M. Grogan, M. C. Reuter, H. H. Bau, S. Kodambaka and F. M. Ross, *Nano Lett.*, 2015, **15**, 5314-5320.
28. D. Alloyeau, W. Dachraoui, Y. Javed, H. Belkahla, G. Wang, H. Lecoq, S. Ammar, O. Ersen, A. Wisnet, F. Gazeau and C. Ricolleau, *Nano Lett.*, 2015, **15**, 2574-2581.
29. N. D. Loh, S. Sen, M. Bosman, S. F. Tan, J. Zhong, C. A. Nijhuis, P. Král, P. Matsudaira and U. Mirsaidov, *Nat. Chem.*, 2017, **9**, 77-82.
30. M. H. Nielsen and J. J. De Yoreo, in *New Perspectives on Mineral Nucleation and Growth: From Solution Precursors to Solid Materials*, eds. A. E. S. Van Driessche, M. Kellermeier, L. G. Benning and D. Gebauer, Springer International Publishing, Cham, 2017, pp. 353-374.
31. N. Ahmad, G. Wang, J. Nelayah, C. Ricolleau and D. Alloyeau, *Nano Lett.*, 2017, **17**, 4194-4201.
32. Y. Zhang, D. Keller, M. D. Rossell and R. Erni, *Chem. Mater.*, 2017, **29**, 10518-10525.
33. J. Wu, W. Gao, J. Wen, D. J. Miller, P. Lu, J.-M. Zuo and H. Yang, *Nano Lett.*, 2015, **15**, 2711-2715.
34. H. Zheng, R. K. Smith, Y.-w. Jun, C. Kisielowski, U. Dahmen and A. P. Alivisatos, *Science*, 2009, **324**, 1309-1312.
35. E. Gachard, H. Remita, J. Khatouri, B. Keita, L. Nadjo and a. Jacqueline Belloni, *New J. Chem.*, 1998, **22**, 1257-1265.
36. N. M. Schneider, M. M. Norton, B. J. Mendel, J. M. Grogan, F. M. Ross and H. H. Bau, *J. Phys. Chem. C*, 2014, **118**, 22373-22382.
37. K. L. Jungjohann, S. Bliznakov, P. W. Sutter, E. A. Stach and E. A. Sutter, *Nano Lett.*, 2013, **13**, 2964-2970.
38. J. M. Yuk, J. Park, P. Ercius, K. Kim, D. J. Hellebusch, M. F. Crommie, J. Y. Lee, A. Zettl and A. P. Alivisatos, *Science*, 2012, **336**, 61-64.
39. S. A. Canepa, B. T. Sneed, H. Sun, R. R. Unocic and K. Molhave, *J. Phys. Chem. C*, 2017, **122**, 2350-2357.
40. H.-G. Liao and H. Zheng, *J. Am. Chem. Soc.*, 2013, **135**, 5038-5043.
41. H.-G. Liao, D. Zherebetskyy, H. Xin, C. Czarnik, P. Ercius, H. Elmlund, M. Pan, L.-W. Wang and H. Zheng, *Science*, 2014, **345**, 916-919.
42. T. H. Moser, H. Mehta, C. Park, R. T. Kelly, T. Shokuhfar and J. E. Evans, *Sci. Adv.*, 2018, **4**.
43. C. Li, X. Chen, H. Liu, J. Fang and X. J. N. R. Zhou, *Nano Res.*, 2018, **11**, 4697-4707.
44. M. H. Nielsen, D. Li, H. Zhang, S. Aloni, T. Y.-J. Han, C. Frandsen, J. Seto, J. F. Banfield, H. Cölfen and J. J. De Yoreo, *Microsc. Microanal.*, 2014, **20**, 425-436.
45. H. Zheng, S. A. Claridge, A. M. Minor, A. P. Alivisatos and U. Dahmen, *Nano Lett.*, 2009, **9**, 2460-2465.
46. B. Michen, C. Geers, D. Vanhecke, C. Endes, B. Rothen-Rutishauser, S. Balog and A. Petri-Fink, *Sci. Rep.*, 2015, **5**, 9793.
47. M. Tanase, J. Winterstein, R. Sharma, V. Aksyuk, G. Holland and J. A. Liddle, *Microsc. Microanal.*, 2015, **21**, 1629-1638.

48. B. H. Kim, J. Yang, D. Lee, B. K. Choi, T. Hyeon and J. Park, *Adv. Mat.*, 2018, **30**, 1703316.
49. P. Abellan, T. J. Woehl, L. R. Parent, N. D. Browning, J. E. Evans and I. Arslan, *Chem. Commun.*, 2014, **50**, 4873-4880.
50. J. M. Grogan, N. M. Schneider, F. M. Ross and H. H. Bau, *Nano Lett.*, 2014, **14**, 359-364.
51. E. A. Ring and N. de Jonge, *Microsc. Microanal.*, 2010, **16**, 622-629.
52. K. L. Klein, I. M. Anderson and N. De Jonge, *J. Microsc.*, 2011, **242**, 117-123.
53. M. H. Nielsen, S. Aloni and J. J. De Yoreo, *Science*, 2014, **345**, 1158-1162.
54. M. E. Holtz, Y. Yu, J. Gao, H. D. Abruña and D. A. Muller, *Microsc. Microanal.*, 2013, **19**, 1027-1035.
55. I. M. Lifshitz and V. V. Slyozov, *J. Phys. Chem. Solids*, 1961, **19**, 35-50.
56. C. J. Johnson, E. Dujardin, S. A. Davis, C. J. Murphy and S. Mann, *J. Mater. Chem.*, 2002, **12**, 1765-1770.
57. S. Barbosa, A. Agrawal, L. Rodríguez-Lorenzo, I. Pastoriza-Santos, R. A. Alvarez-Puebla, A. Kornowski, H. Weller and L. M. Liz-Marzán, *Langmuir*, 2010, **26**, 14943-14950.
58. C. Lofton and W. Sigmund, *Adv. Funct. Mater.*, 2005, **15**, 1197-1208.
59. J. L. Burt, J. L. Elechiguerra, J. Reyes-Gasga, J. Martin Montejano-Carrizales and M. Jose-Yacaman, *J. Cryst. Growth*, 2005, **285**, 681-691.
60. K. A. Tay, F.-X. Coudert and A. Boutin, *J. Chem. Phys.*, 2008, **129**, 054505-054505.
61. K. H. Schmidt, P. Han and D. M. Bartels, *The Journal of Physical Chemistry*, 1992, **96**, 199-206.
62. J. Schnitker and P. J. Rossky, *J. Phys. Chem.*, 1989, **93**, 6965-6969.
63. K. H. Schmidt, P. Han and D. M. Bartels, *J. Phys. Chem.*, 1992, **96**, 199-206.
64. J. Boleininger, A. Kurz, V. Reuss and C. Sönnichsen, *Phys. Chem. Chem. Phys.*, 2006, **8**, 3824-3827.
65. Y. Yin and A. P. Alivisatos, *Nature*, 2005, **437**, 664-670.
66. K. D. Gilroy, H.-C. Peng, X. Yang, A. Ruditskiy and Y. Xia, *Chem. Commun.*, 2017, **53**, 4530-4541.
67. G. Frens, *Nat. Phys. Sci.*, 1973, **241**, 20-22.
68. J. Pérez-Juste, L. M. Liz-Marzán, S. Carnie, D. Y. C. Chan and P. Mulvaney, *Adv. Funct. Mater.*, 2004, **14**, 571-579.
69. C. G. Khoury and T. Vo-Dinh, *The Journal of Physical Chemistry C*, 2008, **112**, 18849-18859.
70. N. Uyeda, M. Nishino and E. Suito, *J. Colloid Interface Sci.*, 1973, **43**, 264-276.
71. H. Hofmeister, in *Handbook of Nanotechnology*, ed. H. Naiwa, American Scientific Publishers, California, USA, 2004.
72. T. Gupta, N. M. Schneider, J. H. Park, D. Steingart and F. M. Ross, *Nanoscale*, 2018, **10**, 7702-7710.
73. J. Berger, Coursey, J. S., Zucker, M. A., Chang, J., *Stopping-Power & Range Tables for Electrons, Protons, and Helium Ions*, NIST, 1988.
74. P. J. M. Smeets, K. R. Cho, R. G. E. Kempen, N. A. J. M. Sommerdijk and J. J. De Yoreo, *Nat. Mater.*, 2015, **14**, 394-399.
75. H. Cho, M. R. Jones, S. C. Nguyen, M. R. Hauwiller, A. Zettl and A. P. Alivisatos, *Nano Lett.*, 2017, **17**, 414-420.
76. J. Kim, D.-H. Kim, S. J. Lee, Y. Rheem, N. V. Myung and H.-G. Hur, *Biosci. Biotechnol. Biochem.*, 2016, **80**, 1478-1483.

TABLE OF CONTENTS

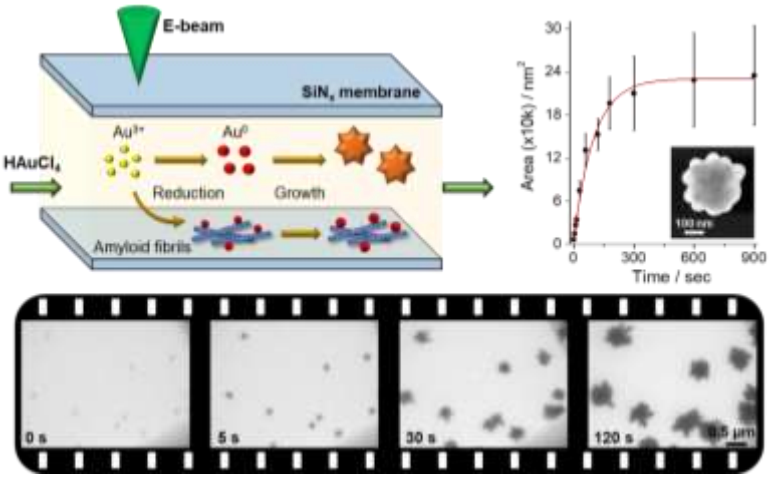
E-beam
SiN$_x$ membrane
Au^{3+}
Au^0
HAuCl$_4$
Reduction
Growth
Amyloid fibrils
Area (x10k) / nm^2
Time / sec
0
6
12
18
24
30
0
300
600
900
100 nm

0 s
5 s
30 s
120 s
0.5 µm